

Wind load simulations and inertia scaling using an industrial robot arm

Boyan R. Klifman

Master thesis

Wind load simulations and inertia scaling using an industrial robot arm

MASTER THESIS

For the degree of Master of Science in Mechanical Engineering at Delft
University of Technology

Boyan R. Klifman

Student number: 4383370

Project duration: March 1, 2021 - September 29, 2021

Thesis committee:

Prof.dr. Frans C.T. van der Helm - TU Delft

Dr. André Schiele - X-Laboratory / TU Delft

Ir. Dabian Y. Oosterloo - X-Laboratory

Dr. Jason. K. Moore. - TU Delft

September 16, 2021

Faculty of Mechanical, Maritime and Materials Engineering (3mE) · Delft University of
Technology

This master thesis was conceived, designed and performed at the Delta Labs B.V., hereafter called the X-Laboratory. The thesis is confidential and cannot be made public until September 15, 2023.



Copyright © X-Laboratory
All rights reserved.

Table of Contents

Preface	ix
Acknowledgements	xi
Abstract	xiii
Wind load simulations and inertia scaling using an industrial robot arm	1
I Introduction	1
II Methods	2
A. Planar computer simulation model	2
B. Admittance control	3
C. Experimentation	5
III Results	6
A. Computer simulation results	6
B. Hardware-in-the-loop (HIL) results	8
IV Discussion	8
V Conclusion	10
A Planar computer simulation model	11
B Admittance control in 6 Degrees of Freedom (DoF)	13
C Experimental conditions	15
References	17
Glossary	19
List of Acronyms	19
List of Symbols	19

List of Figures

1	Schematic representation of the RWS system. The <i>virtual</i> system is the desired situation, where wind loads are acting on a virtual object that has higher inertia than the real object. The <i>real</i> system is the HIL loop setup, where the RWS simulates the wind loads and the inertia. The ObCon controls the position of the object. The RWS is controlled in admittance control based on the feedback of the 6 DoF F/T sensor. The coordinate frames for the world $\{w\}$, the F/T sensor $\{s\}$ and the object $\{r\}$ are also shown.	2
2	The RWS system reduced from 6 DoF to a planar 3 DoF system. The RWS can be seen as a planar three link manipulator when controlled in a vertical plane. Axis A_2 , A_4 and A_6 are active. Furthermore, the kinematic parameters of the planar simplification are indicated. Subscripts a till g represent the links of the RWS. Subscripts 0 till 3 represent the links of the planar model.	2
3	Schematic representation of the planar computer simulation model based on the RWS system. The joint angles of the manipulator links are denoted by $\mathbf{q} = [\theta_1, \theta_2, \theta_3]^T$. Within the joints, there are DC motors and gear trains. In these systems, r denotes the gear ratio, and τ and $\dot{\theta}$ denote the applied torques and velocities, respectively. The moments of inertia around the rotation axis and the friction in the axis are denoted by I and b , respectively. The subscript m is for the motor side before gearing and l for the load side after gearing. Lastly, the ObCon controls the object's pose and the F/T sensor measures the forces and moments between the object and the RWS.	3
4	Block diagram of the admittance control loop for the planar RWS. The measured loads between the object and the end-effector described in the $\{s\}$ frame are captured in $\mathbf{F}_{s\{s\}}$. This signal is first translated by \mathbf{T} to loads in the CoM of the object described in frame $\{r\}$, called $\mathbf{F}_{r\{r\}}$. Hereafter, this signal is described in the $\{w\}$ frame by using the rotation matrix \mathbf{R} . The $\mathbf{F}_{r\{w\}}$ signal together with the user-defined wind forces $\mathbf{F}_{w\{w\}}$ are used in the desired dynamics block to calculate a desired acceleration $\ddot{\mathbf{r}}_{d\{w\}}$. Integrating the acceleration twice gives the Cartesian motion input to the robot $\mathbf{r}_{d\{w\}}$	4

- 5 FBD's for the *virtual* (A.) and the *real* (B.) systems needed in the Desired Dynamics block of the admittance control scheme. Both the virtual and the real systems experience ObCon forces (\mathbf{F}_{cv} and \mathbf{F}_{cr} respectively). The virtual system further experiences wind loads acting on the CoM \mathbf{F}_w and gravitational forces with the virtual mass and virtual gravitational acceleration $m_v g_v$. The real system experiences forces from the robot, which are sensed by the F/T sensor in \mathbf{F}_s . Furthermore, the real system experiences gravitational forces with the real mass and the standard gravitational acceleration $m_r g$. Lastly, the virtual inertia parameters are higher than the real inertia parameters ($m_v > m_r, I_v > I_r$). 4
- 6 Block diagram for the initial experiment on the computer simulation model to verify the simulation abilities of the admittance control loop. The inputs for the experiment are the object trajectory for the ObCon $\mathbf{p}_o(t)$, the user-defined wind loads $\mathbf{F}_w(t)$ and the virtual inertia parameters m_v, I_v and g_v . The outputs are the forces the ObCon exerts on the objects in the virtual and real situation, $\mathbf{F}_{cv}(t)$ and $\mathbf{F}_{cr}(t)$ respectively. The RMSE between $\mathbf{F}_{cv}(t)$ and $\mathbf{F}_{cr}(t)$ in x, y and z directions are the final outputs of the experiment. 5
- 7 Picture of the HIL setup of the RWS. Attached to the end-effector of the RWS is a 6 DoF F/T sensor. Attached to this sensor is a real object with parameters $m_r = 0.934$ kg, $I_r = 0.0123$ kgm², $d_x = -2.00e-5$ m, $d_y = 0.0771$ m. Note that there is no ObCon available on the HIL setup. 6
- 8 Block diagram for the second experiment on the HIL setup to verify the simulation abilities of the admittance control loop on the HIL setup. The inputs for the experiment are the user-defined wind loads $\mathbf{F}_w(t)$ and the virtual inertia parameters $m_v = 116.75$ kg, $I_v = 38.51$ kgm² and $g_v = 0.0$ m/s². The outputs are the trajectories of the object's CoM in the virtual situation $\mathbf{r}_v(t)$ and in the real situation with the RWS $\mathbf{r}_r(t)$. The RMSE between $\mathbf{r}_v(t)$ and $\mathbf{r}_r(t)$ are the final outputs of the experiment. 6
- 9 The results for the first experiment on the computer simulation model. The ObCon forces in the virtual environment \mathbf{F}_{cv} and the admittance controlled environment \mathbf{F}_{cr} are compared to each other by taking the RMSE of the signals over time. A block diagram of the experiment can be seen in Fig. 6. 7
- 10 The results for the second experiment on the computer simulation model. The average RMSE between the ObCon forces in the virtual environment \mathbf{F}_{cv} and the admittance controlled environment \mathbf{F}_{cr} are plotted against different sample times of the RWS T_{RWS} . This analysis is executed for four different sample times of the ObCon T_{ObCon} 7
- 11 The results for the third experiment on the computer simulation model. The average RMSE between the ObCon forces in the virtual environment \mathbf{F}_{cv} and the admittance controlled environment \mathbf{F}_{cr} are plotted against different amounts of virtual inertia (m_v, I_v). This analysis is executed for five different amounts of real object inertia (m_r, I_r), which are indicated in the graphs by the dashed lines. In this experiment there are no wind loads simulated and the sample time is $T_{RWS} = 0.005$ s. The numerical values of the results can be found in table I. . . 7
- 12 The results for the fourth experiment on the computer simulation model. The range of possible virtual inertias m_v and I_v are plotted against the sample times for the RWS T_{RWS} . The shown results are obtained in simulations with a real inertia of $m_r = 14.50$ kg and $I_r = 0.54$ kg². 7
- 13 The results for the fifth experiment on the computer simulation model. The average RMSE between the ObCon forces in the virtual environment \mathbf{F}_{cv} and the admittance controlled environment \mathbf{F}_{cr} are plotted against different amounts of virtual inertia (m_v, I_v). This analysis is executed for five different amounts of real object inertia (m_r, I_r), which are indicated in the graphs by the dashed lines. In this experiment there are wind loads simulated. Furthermore, the RWS sample time is $T_{RWS} = 0.005$ s. The numerical values of the results can be found in table II. 7

-
- 14 The results for the second experiment on the HIL setup. The virtual trajectory $r_v(t)$ and real trajectory $r_r(t)$ caused by sinusoidal wind loads on a 0-g environment are plotted. Also, the detrended real signal $r_{r,\text{detrend}}(t)$ is plotted. This signal is detrended with the standard drift measured when no wind loads are applied. The sample frequency $\frac{1}{T_{\text{RWS}}}$ for this experiment was 2333 Hz. The RMSE in x , in y and in φ are the final metrics for this experiment. 8
- 15 The results for the third and last experiment on the HIL setup. The sample time of the admittance control loop T_{RWS} is plotted against the normalized error. This error is the RMSE between the virtual object trajectory $r_v(t)$ and the real object trajectory $r_r(t)$. The results from the computer simulation model (Fig. 10) are also plotted. The normalized RMSE for both the HIL setup and the computer simulation is found by dividing all RMSE by the minimal RMSE. 8

List of Tables

I	Numerical results for the third experiment on the computer simulation model from Fig. 11.	7
II	Numerical results for the fifth experiment on the computer simulation model from Fig. 13.	7

Preface

For obtaining the degree of master of science at the Delft University of Technology (TU Delft), faculty of Mechanical, Maritime and Materials Engineering (3mE), masters study Mechanical Engineering (ME), track BioMechanical Design (BMD), specialization BioRobotics (BR), I, Boyan Klifman, am doing my master thesis research project at X-Laboratory. X-Laboratory is a high-tech robotics engineering firm - specialized in building "one-off" and "highly automated" equipment for the maritime and offshore energy industries. X-Laboratory gave me the opportunity to research whether an industrial robot arm could be used to simulate wind loads on an object. This thesis will elaborate on the proceedings of this research.

This master thesis consists of a scientific paper and multiple appendices. The paper should give a good overview of the research for the interested reader. It is build up as a scientific paper where the *introduction* states the problem. Hereafter, the *methods* used for solving this problem are explained. Computer simulation experiments and Hardware-in-the-loop (HIL) experiments are executed to answer the main problem. *Results* for these experiments are shown and hereafter *Discussed*. Lastly, *conclusions* are drawn based on the experimental results.

The reader that requires more details and wants to reproduce or continue the work can use the appendices. Appendix A elaborates on the computer simulation model that is built. The reader that wants to continue this research can use Appendix B. It explains the extension of the study from 3 Degrees of Freedom (DoF) to 6 DoF. Lastly, Appendix C gives the exact experimental conditions used, mainly meant for the reader who wants to reproduce the research.

This is a special version where confidential information from X-laboratory is taken away. The full uncensored version can be requested at: info@deltaxlab.com

Acknowledgements

I want to thank the people of X-Laboratory for facilitating my literature review and thesis of my master study. The daily supervision by Dabian Oosterloo taught me a lot about multiple engineering subjects and about the process of writing a scientific report. Also, the interesting conversations and discussions with both Dabian Oosterloo and André Schiele inspired me to research new fields of study. All other colleagues at X-Laboratory I would like to thank for their help and the laughs we had during the past nine months. Also, I would like to thank professor Frans van der Helm for his supervision. He gave me great feedback on my work and my writing. I learned a great deal from this. Lastly, I would like to thank Jason Moore for reviewing my thesis and participating in the committee.

Moreover, I would like to thank my family and friends for their support over the complete duration of my studies. With their love, laughs and support, I managed to stay positive and motivated. They made these past couple of years a great time of my life.

Delft, University of Technology
September 16, 2021

Boyan R. Klifman

Abstract

Existing wind load simulators such as wind tunnels and fans have multiple disadvantages, especially when used in a scaled-down environment. This paper proposes to simulate wind loads by using an admittance-controlled industrial robot arm rigidly attached to a research object. Admittance control should make it possible to simulate wind loads and a specific amount of inertia that is higher than the inertia of the original research object. The goal is to verify whether an admittance-controlled industrial robot arm is suitable for wind load and inertia simulations and what the limitations of this simulation method are. The scope of this research is limited to three Degrees of Freedom. First, the admittance controller is tested on a computer simulation model before execution on a Hardware-in-the-loop setup. It is found that an admittance-controlled robot arm is well capable of simulating both wind loads and a specific amount of inertia. However, there are some limitations. The motion controller of the industrial robot should be able to change the end-effector position within a frequency of 50 Hz. Frequencies above 333 Hz result in the most accurate simulations. The upper range of inertia that can be simulated is restricted by the maximum joint torques the robot can apply. The lower range is restricted by the inertia of the real object, the applied wind loads, and the sampling frequency of the admittance control loop.

Wind load simulations and inertia scaling using an industrial robot arm

Boyan R. Klifman¹

Abstract—Existing wind load simulators such as wind tunnels and fans have multiple disadvantages, especially when used in a scaled-down environment. This paper proposes to simulate wind loads by using an admittance-controlled industrial robot arm rigidly attached to a research object. Admittance control should make it possible to simulate wind loads and a specific amount of inertia that is higher than the inertia of the original research object. The goal is to verify whether an admittance-controlled industrial robot arm is suitable for wind load and inertia simulations and what the limitations of this simulation method are. The scope of this research is limited to three Degrees of Freedom. First, the admittance controller is tested on a computer simulation model before execution on a Hardware-in-the-loop setup. It is found that an admittance-controlled robot arm is well capable of simulating both wind loads and a specific amount of inertia. However, there are some limitations. The motion controller of the industrial robot should be able to change the end-effector position within a frequency of 50 Hz. Frequencies above 333 Hz result in the most accurate simulations. The upper range of inertia that can be simulated is restricted by the maximum joint torques the robot can apply. The lower range is restricted by the inertia of the real object, the applied wind loads, and the sampling frequency of the admittance control loop.

Index Terms—Admittance control, Wind simulation, dynamics simulation, inertia scaling, multi-body dynamics, Hardware-In-the-Loop (HIL) testing

I. INTRODUCTION

FOR Hardware-In-the-Loop (HIL) testing of novel products, it is important to simulate environmental conditions accurately. For example, in [1] they test a HIL scaled-down setup of a floating wind turbine. The scale model is placed in an ocean basin to simulate the hydrodynamic loads. At the same time, a large wind tunnel simulates the aerodynamic loads. There are also other strategies to simulate wind loads on a scale model. Some of them are summarized in [2]. One of the earliest and most straightforward methods is a system of pulleys, cables, and a mass that can apply a force in the direction of the wind. Other methods are fans mounted next to the model or a fan mounted onto the model.

These wind simulation methods have disadvantages. When using a pulley system, it is impossible to simulate the complete spectrum of wind loading. Moreover, the pulley system adds extra inertia. Fans mounted onto the model can simulate the frequencies of the wind loads but still have the problem of added inertia. No extra inertia is added to the model when making use of wind tunnels. However, in wind tunnels, a

precise scale model of the superstructure is needed. Another disadvantage of wind tunnels is the size. For relatively large models, large and expensive wind tunnels are needed. Mounting fans next to the model does not have this problem. However, the wind's flow regime must be considered, which means that the Reynolds number should stay constant over the scaling factor. This necessitates high wind speeds in the scaled-down environment. Fans next to the model are not able to achieve these high wind speeds. A disadvantage for all mentioned methods is that there is no precise knowledge of the applied wind loads. This is not desirable in highly quantitative HIL experimentation.

In this paper, the objective is to simulate wind loads on an object in a scaled-down environment. An example of this application could be simulating wind loading on containers carried by a crane. Due to the issues found in the wind simulation strategies from [2] a novel method is proposed to simulate wind loads, namely, simulation by making use of an industrial robot arm. This system will be called the Robotic Wind Simulator (RWS). The hypothesis is that by rigidly attaching the end-effector to the object and adequately controlling the robot, it is possible to apply external loads and simulate a desired and higher amount of inertia of the object.

The idea for the RWS comes from research in space engineering, where they use industrial robot arms to simulate 0-g spacecraft dynamics in a 1-g laboratory. In [3] a small test spacecraft attached to the end-effector is controlled in such a way to simulate the dynamic behaviour of a larger spacecraft in microgravity. In [4] and [5] they use the same method to simulate the dynamics of two spacecraft and the interaction between both for testing new On-Orbit Servicing (OOS) missions. Furthermore, in [6] the same HIL OOS robotic simulators as in [5] are used to simulate the relative dynamics between the two spacecraft. This relative description increases the workspace of the simulations. These researches control the robot in admittance control to simulate the dynamics of satellites. A Force/Torque (F/T) sensor measures the forces and torques between the robot and the test satellite. Based on these forces, the robot admits a certain motion to the test satellite. This motion is calculated based on the desired Equations of Motion (EoM) of the satellite dynamics.

The RWS proposed in this paper adds an external wind load simulation to the desired dynamics simulation strategy used in space engineering. This will result in a novel wind simulation technique that can be used for HIL scale model testing. The new method has advantages over the original methods for simulating wind loads. First of all, no precise model of the superstructure is needed while still being able to

¹ B.R. Klifman is a master student BioMechanical Design, specialization BioRobotics, at the Delft University of Technology.
E-mail: boyanklifman@gmail.com

test with the desired amount of inertia. Secondly, Froude's scaling laws instead of Reynolds' can be used due to the absence of flow. This means that a full-scale wind load data set can directly be scaled down according to Froude's laws. Furthermore, the RWS can simulate the complete spectrum of wind loading instead of only the mean load. Lastly, the RWS is suitable for highly quantitative experimentation due to the precise knowledge of the applied wind loads.

The main problem to solve in this paper is: "Can an admittance-controlled industrial robot arm be used to simulate wind loads on an object while also simulating a desired and higher amount of inertia of that object, and what are the limitations of this method?" Section II explains the steps taken to solve this problem. The scope of this research is reduced to 3 Degrees of Freedom (DoF) to simplify the implementation. The admittance controller is first tested on a 3 DoF computer simulation model before executing it on a HIL setup. Section III describes the results of the computer simulation study and the HIL study. In section IV the results are discussed, and the limitations of the admittance control strategy are stated. Lastly, in section V conclusions for this research are drawn.

II. METHODS

A schematic representation of the RWS system can be seen in Fig. 1. The left figure shows the *virtual* system that is to be simulated. The right figure shows the *real* HIL RWS system. The latter consists of an industrial robot arm with an object rigidly connected to the end-effector. An 6 DoF F/T sensor is attached between the end-effector of the RWS and the object. There are two control structures from two different robots active in the whole system. The Object Controller (ObCon), represented by the KUKA KR120 in Fig. 1, controls the position of the object. The RWS applies wind loads to the object and changes the inertia of the object. The goal is to control the RWS in such a way that the ObCon must behave like it is acting on a virtual object that experiences wind loads and has higher inertia than the real object. Both the wind loads and the desired inertia are user-defined.

The admittance control strategy was first developed for a simplified planar representation of the RWS system. This reduction from 6 DoF to 3 DoF is shown in Fig. 2. The robot arm in the planar model is a three-link manipulator with a three DoF end-effector. This configuration is chosen because the RWS can be reduced to a three-link manipulator when controlled in a vertical plane. Reducing the DoF of the system simplifies the dynamic equations and the frame transformations, making the theory easier to understand. Subsequent research should elaborate on the translation of the theory from 3 DoF to 6 DoF. The first step taken in this research is developing a computer simulation model of the planar RWS that can be used for testing.

A. Planar computer simulation model

Fig. 3 shows a schematic representation of the computer simulation model. The kinematic and dynamic parameters of the simulation model are based as much as possible on the parameters of the actual robot.

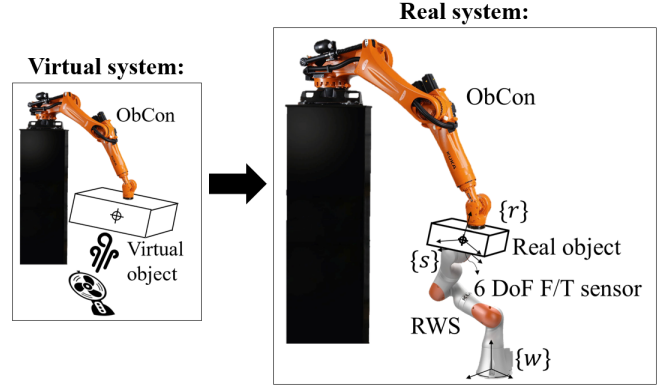


Fig. 1. Schematic representation of the RWS system. The *virtual* system is the desired situation, where wind loads are acting on a virtual object that has higher inertia than the real object. The *real* system is the HIL loop setup, where the RWS simulates the wind loads and the inertia. The ObCon controls the position of the object. The RWS is controlled in admittance control based on the feedback of the 6 DoF F/T sensor. The coordinate frames for the world $\{w\}$, the F/T sensor $\{s\}$ and the object $\{r\}$ are also shown.

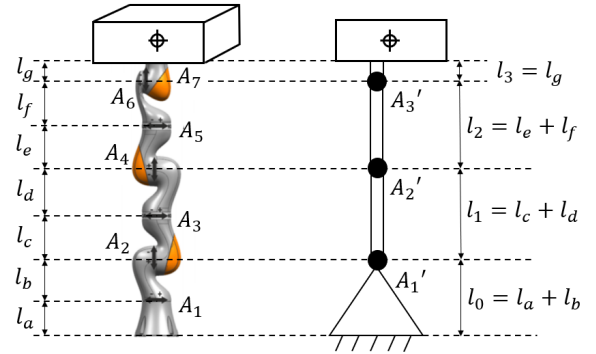


Fig. 2. The RWS system reduced from 6 DoF to a planar 3 DoF system. The RWS can be seen as a planar three link manipulator when controlled in a vertical plane. Axis A_2 , A_4 and A_6 are active. Furthermore, the kinematic parameters of the planar simplification are indicated. Subscripts a till g represent the links of the RWS. Subscripts 0 till 3 represent the links of the planar model.

Direct Current (DC) motors actuate the joints of the planar manipulator. The DC motor model from [7] and [8] is used. This model includes an electrical excitation system with back electromotive forces (emf). Also, the model contains a gear train, which results in the fact that the effective inertia of the DC motors must be taken into account. The model further incorporates friction within the motors and friction within the joints themselves.

Appendix A-I explains the kinematics of the computer simulation model in detail. The Forward Kinematics (FK) equations can translate three joint angles to an end-effector pose in 3 DoF. The Jacobian matrix $J(q)$ is the partial derivative of the FK equations over the joint angles q . This Jacobian can translate joint velocities to end-effector velocities when the joint angles are known. The inverse Jacobian $J^{-1}(q)$ can translate end-effector velocities to joint velocities.

Appendix A-II explains the dynamic EoM of the computer simulation model in detail. They are derived by making use of the TMT method [9]. The final EoM can be written in the

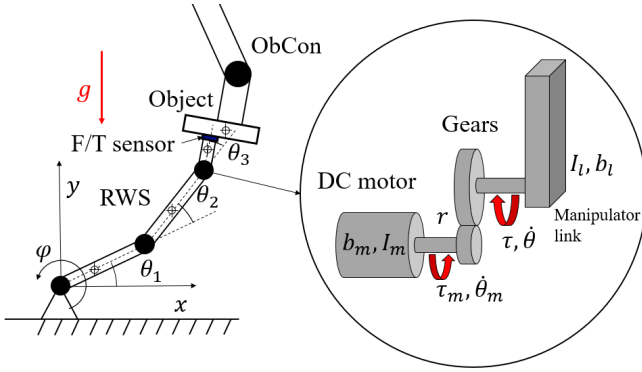


Fig. 3. Schematic representation of the planar computer simulation model based on the RWS system. The joint angles of the manipulator links are denoted by $\mathbf{q} = [\theta_1, \theta_2, \theta_3]^T$. Within the joints, there are DC motors and gear trains. In these systems, r denotes the gear ratio, and τ and $\dot{\theta}$ denote the applied torques and velocities, respectively. The moments of inertia around the rotation axis and the friction in the axis are denoted by I and b , respectively. The subscript m is for the motor side before gearing and l for the load side after gearing. Lastly, the ObCon controls the object's pose and the F/T sensor measures the forces and moments between the object and the RWS.

form,

$$\mathbf{M}(\mathbf{q})\ddot{\mathbf{q}} = \boldsymbol{\tau}(\mathbf{V}_a, \dot{\mathbf{q}}) - \mathbf{C}(\mathbf{q}, \dot{\mathbf{q}})\dot{\mathbf{q}} - \mathbf{G}(\mathbf{q}) \quad (1)$$

Matrix $\mathbf{M}(\mathbf{q})$ is the inertia matrix as a function of the joint angles. Vector $\mathbf{C}(\mathbf{q}, \dot{\mathbf{q}})$ contains the Coriolis and centrifugal forces as a function of joint angles and joint velocities. The vector $\mathbf{G}(\mathbf{q})$ captures the gravitational forces as a function of joint angles, and $\boldsymbol{\tau}(\mathbf{V}_a, \dot{\mathbf{q}})$ are the motor torques after gearing as a function of armature voltages and joint velocities. It is important to note that the F/T sensor is modelled by adding three extra constraints in the TMT EoM. Appendix A-II elaborates on these constraints. Quantization and noise are added to the F/T sensor signal to make it more realistic.

The EoM of the planar manipulator are implemented into a model-based tool. Integrator blocks calculate the joint velocities $\dot{\mathbf{q}}$ and joint angles \mathbf{q} from the joint accelerations $\ddot{\mathbf{q}}$. These accelerations are obtained with the forward dynamics equations described in equation (1). The sum of the systems' potential and kinetic energy is plotted to check whether the EoM are correctly calculated and implemented. This resulted in a constant sum of energies over time.

The actual RWS comes with a control cabinet that can control the motion of the end-effector. However, for the planar computer simulation model, this motion controller must be developed. The Cartesian space motion controller consists of two types of controllers. The first ones are PID controllers that can control the torques applied by the DC motors. These are needed to compensate for the nonlinear effects caused by the back-emf of the motors. Appendix A-III contains more information about the joint-torque controllers. It is important to note that the joint-torque controllers must run with a higher sample frequency and a higher bandwidth than the general motion control loop.

The general motion control loop used in the computer simulation model is called: "computed-torque control in workspace". This control loop is based on [10] and it uses the

dynamic model from equation (1) to feed-forward the dynamics of the manipulator. The loop utilizes the Jacobian $\mathbf{J}(\mathbf{q})$, the inverse Jacobian $\mathbf{J}^{-1}(\mathbf{q})$ and the FK of the manipulator to translate joint space data into Cartesian space data. The controller is sensitive for singular configurations due to the use of the inverse Jacobian. The Jacobian is not full rank anymore at singular configurations, which means that it becomes not invertible. To partially overcome this problem, the Singularity-robust pseudo-inverse from [11] is used. Furthermore, the controller gains are tuned around the optimal manipulability angles of the joints based on Yoshikawa's manipulability measure [12]. Appendix A-III elaborates on the Computed torque control in workspace loop and the tuning of the controller gains.

Another robot and control loop is also active, Namely, the ObCon. The ObCon in the computer simulation model is also a computed torque controller. It changes the object's pose by applying forces to the Centre of Mass (CoM) of the object. Appendix A-III depicts a block diagram and detailed description of the ObCon. The ObCon must eventually ensure that the object follows a trajectory while the RWS is disturbing the object with wind loads and a change in inertia.

B. Admittance control

The RWS applies wind forces and increases the object's inertia by using an admittance control loop. This is also the type of control used for simulating desired dynamics of spacecraft in [3], [4], [5] and [6]. Admittance controllers sense a force and 'admit' a certain motion. This is opposite to Impedance controllers that sense a position error and 'impede' the motion with force according to a certain impedance law. These principles are explained in the origin papers for impedance and admittance control by Neville Hogan [13][14][15]. He explained that in most cases, the environment should be considered an admittance, which indicates that an admittance controller can be used to simulate an environment with higher inertia of the object and wind loads acting on that object.

Fig. 4 shows the admittance control loop used for the planar representation of the RWS. The F/T sensor measures forces in the x and y direction and a moment around the z direction. This data is fed back into the 'Desired Dynamics' block. This block calculates the motion reaction that the manipulator should admit to the object based on the 'desired' virtual inertia of the object and the 'desired' virtual wind loads \mathbf{F}_w . The output of the Desired Dynamics block is a Cartesian motion for the object that the manipulator's motion controller must execute.

Two dynamic systems must be defined to calculate the object's motion. The system with the desired higher inertia and the user-defined wind loads is called the *virtual* system. The actual RWS system with the robot arm attached is called the *real* system. Fig. 5 depicts the Free Body Diagrams (FBD) of both systems.

The forces acting on the *virtual* system (A.) are the control forces of the ObCon \mathbf{F}_{cv} , the gravitational forces with a virtual gravitational acceleration g_v , and the wind loads acting on the CoM \mathbf{F}_w . The virtual mass is denoted by m_v , and the virtual

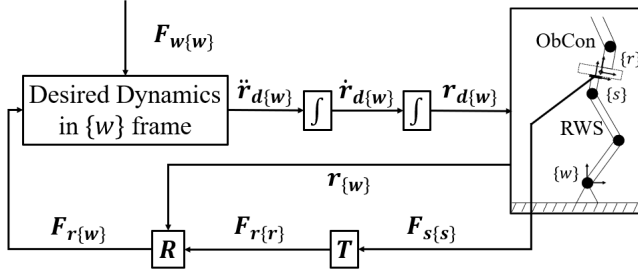


Fig. 4. Block diagram of the admittance control loop for the planar RWS. The measured loads between the object and the end-effector described in the $\{s\}$ frame are captured in $F_{s\{s\}}$. This signal is first translated by T to loads in the CoM of the object described in frame $\{r\}$, called $F_{r\{r\}}$. Hereafter, this signal is described in the $\{w\}$ frame by using the rotation matrix R . The $F_{r\{w\}}$ signal together with the user-defined wind forces $F_w\{w\}$ are used in the desired dynamics block to calculate a desired acceleration $\ddot{r}_d\{w\}$. Integrating the acceleration twice gives the Cartesian motion input to the robot $r_d\{w\}$.

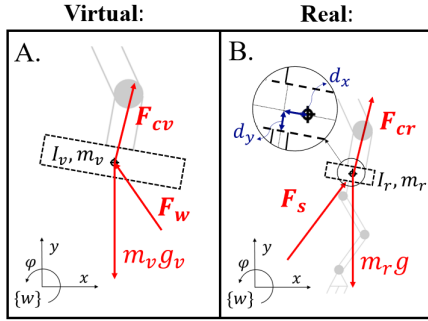


Fig. 5. FBD's for the *virtual* (A.) and the *real* (B.) systems needed in the Desired Dynamics block of the admittance control scheme. Both the virtual and the real systems experience ObCon forces (F_{cv} and F_{cr} respectively). The virtual system further experiences wind loads acting on the CoM F_w and gravitational forces with the virtual mass and virtual gravitational acceleration $m_v g_v$. The real system experiences forces from the robot, which are sensed by the F/T sensor in F_s . Furthermore, the real system experiences gravitational forces with the real mass and the standard gravitational acceleration $m_r g$. Lastly, the virtual inertia parameters are higher than the real inertia parameters ($m_v > m_r$, $I_v > I_r$).

mass moment of inertia by I_v . The EoM of the virtual system described in the world frame $\{w\}$ are then defined by,

$$\begin{bmatrix} m_v & 0 & 0 \\ 0 & m_v & 0 \\ 0 & 0 & I_v \end{bmatrix} \begin{bmatrix} \ddot{x}_v \\ \ddot{y}_v \\ \ddot{\varphi}_v \end{bmatrix} = \begin{bmatrix} F_{x,cv} + F_{x,w} \\ F_{y,cv} + F_{y,w} - m_v g_v \\ M_{z,cv} + M_{z,w} \end{bmatrix} \quad (2)$$

The forces acting on the *real* (B.) system are the ObCon forces F_{cr} , the gravitational forces with the standard gravitational acceleration g and the forces from the RWS measured by the F/T sensor $F_{s\{s\}}$. Note that the latter is not acting on the CoM of the object and is not described in the world frame $\{w\}$. Therefore, a transformation T and a rotation R are needed to translate it to $F_{r\{w\}}$. The mass and mass moments of inertia of the real system are denoted by m_r and I_r , respectively. The EoM of the real system described in the world frame $\{w\}$ are then described by,

$$\begin{bmatrix} m_r & 0 & 0 \\ 0 & m_r & 0 \\ 0 & 0 & I_r \end{bmatrix} \begin{bmatrix} \ddot{x}_r \\ \ddot{y}_r \\ \ddot{\varphi}_r \end{bmatrix} = RT \begin{bmatrix} F_{x,s} \\ F_{y,s} \\ M_{z,s} \end{bmatrix} + \begin{bmatrix} F_{x,cr} \\ F_{y,cr} - m_r g \\ M_{z,cr} \end{bmatrix} \quad (3)$$

Where,

$$RT = \begin{bmatrix} \cos(\varphi_r) & -\sin(\varphi_r) & 0 \\ \sin(\varphi_r) & \cos(\varphi_r) & 0 \\ 0 & 0 & 1 \end{bmatrix} \begin{bmatrix} 1 & 0 & 0 \\ 0 & 1 & 0 \\ d_y & -d_x & 1 \end{bmatrix} \quad (4)$$

The angle φ_r represents the orientation of the real object. This means that the pose of the end-effector $r_{\{w\}}$ must be fed back to R . The lengths d_x and d_y are the distances between the sensor frame $\{s\}$ and the object CoM frame $\{r\}$ described in the $\{s\}$ frame.

Dynamic similarity between the real and virtual systems can be achieved by admitting a desired motion to the real object with the robotic manipulator. The desired acceleration can be obtained by subtracting equation 3 from equation 2. Which means subtracting the EoM of the real system from the EoM of the virtual system. If the virtual and real systems have equivalent dynamics, the ObCon forces in both systems must be identical ($F_{cv} = F_{cr}$). Which eventually results in the EoM for the desired dynamics, all described in the $\{w\}$ frame,

$$M_\Delta \ddot{r}_d = F_w - RT F_s + G_\Delta \quad (5)$$

$$\begin{bmatrix} m_v - m_r & 0 & 0 \\ 0 & m_v - m_r & 0 \\ 0 & 0 & I_v - I_r \end{bmatrix} \begin{bmatrix} \ddot{x}_d \\ \ddot{y}_d \\ \ddot{\varphi}_d \end{bmatrix} = \begin{bmatrix} F_{x,w} \\ F_{y,w} \\ M_{z,w} \end{bmatrix} - RT \begin{bmatrix} F_{x,s} \\ F_{y,s} \\ M_{z,s} \end{bmatrix} + \begin{bmatrix} 0 \\ -m_v g_v + m_r g \\ 0 \end{bmatrix} \quad (6)$$

These equations can be solved for \ddot{r}_d in every loop of the admittance control scheme. The \ddot{r}_d signal can be integrated twice to get the desired object velocity \dot{r}_d and the desired object pose r_d . The latter will be given as a reference to follow for the motion controller of the robotic arm.

The admittance control loop has now been explained for the planar RWS. The planar representation is the scope of this research. An extension to 6 DoF should be tested in subsequent research. However, Appendix B already explains the admittance control structure needed in 6 DoF. There are a few significant differences between the admittance controllers in 3 DoF and 6 DoF. First, the desired dynamics equations in 6 DoF contain a Coriolis and centrifugal term that is not present in 3 DoF. Secondly, velocities and forces/moments are in 6 DoF described by twists and wrenches, respectively. Transforming these twists and wrenches between different frames is done by using transformation matrices and adjoint mappings. This makes the admittance control loop more complex. Lastly, integrating the output of the desired dynamics block is less straightforward in 6 DoF. While integrating this signal, the screw theory described in [16] must be taken into account.

Appendix B contains more details about the admittance control loop in 6 DoF.

For the rest of this research, the admittance control loop in 3 DoF is tested. Whether the admittance-controlled robot arm can simulate the desired wind dynamics must be verified in experiments. The following section explains the methods for executing these experiments.

C. Experimentation

The goal of the experiments is to check whether the admittance-controlled RWS can simulate the desired dynamics. Moreover, limitations of this method must be found. Limitations in terms of controller bandwidth, maximum and minimum virtual inertia, and wind loads' influence are researched. Experimental research is first executed on the computer simulation model. Hereafter, experiments on the 3 DoF HIL system must validate the findings of the computer simulation study in the real world.

1) *Computer simulation experiments:* All computer simulation experiments are executed in a model-based tool. The *first* experiment is a general test of whether the admittance controller can simulate desired dynamics and wind loads. This can be checked by comparing the ObCon forces in the virtual system F_{cv} and in the admittance-controlled real system F_{cr} . Fig. 6 shows a block diagram of this initial experiment. Inputs for this experiment are an object trajectory commanded to the ObCon $p_o(t)$ and wind loads over time $F_w(t)$. Other inputs are the virtual parameters for the inertia (m_v, I_v) and the virtual gravitational acceleration (g_v). Appendix C contains more details about the inputs for this initial experiment. Both the virtual and the real systems are simulated in a model-based tool to obtain the ObCon forces over time. If the required forces to execute the trajectory are equal, this means that the inertias of the systems are the same and that the applied wind loads on the systems are the same. Therefore, the Root Mean Squared Error (RMSE) between the virtual ObCon forces F_{cv} and the real ObCon forces F_{cr} is taken as a metric that indicates whether the simulation is successful.

The *second* experiment on the computer simulation model must indicate the limitation in terms of sample time. Within the model, there are multiple sample times active. Such as the sample time of the ObCon $T_{ObCon} = 0.01$ s, the sample time of the motion controller and the admittance control loop T_{RWS} , the sample time of the joint torque controllers $T_{joint} = \frac{1}{10} \cdot T_{RWS}$ and the sample time of the forward dynamics calculations $T_{dyn} = 1e-5$ s. The goal is to find the range of T_{RWS} that results in successful desired dynamics simulations. The benefit of knowing this range is that it indicates how fast the motion controller of a robot must be to simulate the wind dynamics successfully. This can be helpful if, for example, another robot is to be used for the same application. The first experiment (Fig. 6) is executed multiple times for different sample times, and the average RMSE of x, y and z are saved. It is hypothesized that T_{ObCon} can have influence on the range of T_{RWS} . To check this influence the described experiment is executed for four different T_{ObCon} , namely 0.001 s, 0.005 s, 0.01 s and 0.02 s.

Computer simulation experiment:

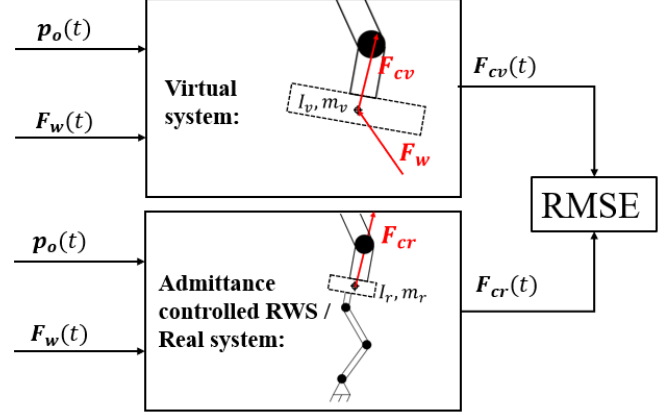


Fig. 6. Block diagram for the initial experiment on the computer simulation model to verify the simulation abilities of the admittance control loop. The inputs for the experiment are the object trajectory for the ObCon $p_o(t)$, the user-defined wind loads $F_w(t)$ and the virtual inertia parameters m_v, I_v and g_v . The outputs are the forces the ObCon exerts on the objects in the virtual and real situation, $F_{cv}(t)$ and $F_{cr}(t)$ respectively. The RMSE between $F_{cv}(t)$ and $F_{cr}(t)$ in x, y and z directions are the final outputs of the experiment.

The *third* experiment must indicate the limitation in terms of virtual inertia (m_v, I_v). In other words, what are the minimum and maximum virtual inertia that the RWS can simulate? It is hypothesised that these ranges are dependent on the inertia of the real object (m_r, I_r) and the applied wind loads. This third experiment analyses the dependency on the real object inertia. The first experiment (Fig. 6) is executed multiple times but now without inputting any wind loads ($F_w(t) = 0$). Every run executes another combination of real and virtual inertia, and the average RMSE are saved.

The *fourth* experiment must indicate the dependency between T_{RWS} and the range of possible virtual inertia. This is done by executing the third experiment multiple times for different sample times. Every run of the experiment, the upper and lower ranges of the virtual inertia simulation are saved.

In the *fifth* and last experiment on the computer simulation model, the influence of the wind loads is analysed. The exact process as in the third experiment is executed but now with the application of wind loads. The same wind load trajectory $F_w(t)$ as in experiments 1 and 2 is applied.

Besides experimental research on the computer simulation model, also experiments are executed on a HIL setup.

2) *HIL experiments:* Fig. 7 shows a picture of the HIL setup. The real object parameters are $m_r = 0.934$ kg, $I_r = 0.0123$ kgm², $d_x = -2.00e-5$ m, $d_y = 0.0771$ m. The RWS is controlled in motion control by making use of an interface with the model-based tool. This interface contains .java files that can be uploaded to the RWS' control cabinet. These files control the Cartesian position of the RWS end-effector. The model-based tool sends User Datagram Protocol (UDP) packages containing the desired pose of the end-effector to the control cabinet. The control cabinet sends Cartesian pose feedback to the model-based tool, also using the UDP. The admittance control loop needs F/T feedback. Therefore, a

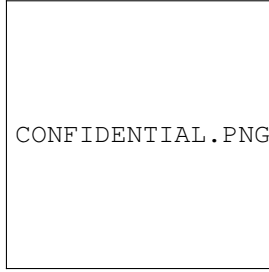


Fig. 7. Picture of the HIL setup of the RWS. Attached to the end-effector of the RWS is a 6 DoF F/T sensor. Attached to this sensor is a real object with parameters $m_r = 0.934$ kg, $I_r = 0.0123$ kgm², $d_x = -2.00e-5$ m, $d_y = 0.0771$ m. Note that there is no ObCon available on the HIL setup.

model-based tool interface for the F/T sensor is written. An code in C language asks the sensor for data and translates this data to the correct $F_{s\{s\}}$ signal.

With the motion controller and the F/T feedback available, it is possible to implement the admittance control loop seen in Fig. 4 on the HIL setup. Unfortunately, it is impossible to execute the same experiments as in the computer simulation study because there is no ObCon available yet on the HIL setup. Therefore, other experiments must verify whether the dynamics simulations are successful.

The *first* experiment on the HIL setup is a 0-g simulation of a virtual object. Without an ObCon, 0-g simulations are the only ones possible because the object would otherwise accelerate downwards. The virtual inertia parameters are set to: $m_v = 116.75$ kg, $I_v = 38.51$ kgm² and $g_v = 0.0$ m/s². The real object should then behave as if it is a much larger object floating in space. The object is manipulated by hand to see the effects of external forces. The results of this first experiment are not expressed in numbers but will be shown in a video.

The *second* experiment on the HIL setup is a numerical experiment. Fig. 8 shows a block diagram of this experiment. Again a 0-g simulation is executed because there is no ObCon available. However, wind loads are added to the simulation in this second experiment, and the object should not be manipulated by hand. Sinusoidal and relatively small wind loads are used to ensure that the object does not fly out of the workspace of the RWS. Appendix C shows more details about these applied wind loads. External loads acting on a virtual object in 0-g cause a certain trajectory of the object's CoM. The trajectories in the virtual and the real situation are compared to each other to check whether the wind dynamics simulation is successful. The metric taken is the RMSE between the virtual object trajectory $r_v(t)$ and the real object trajectory $r_r(t)$.

The *third* and last experiment on the HIL setup is a search for the range of possible sample times of the admittance control loop, called T_{RWS} . This HIL experiment is comparable to the second experiment on the computer simulation model. The experiment seen in Fig 8 is executed multiple times for different T_{RWS} . Every iteration, the average RMSE is saved to see the relationship between sample time and simulation error.

The five experiments on the computer simulation model and

HIL experiment:

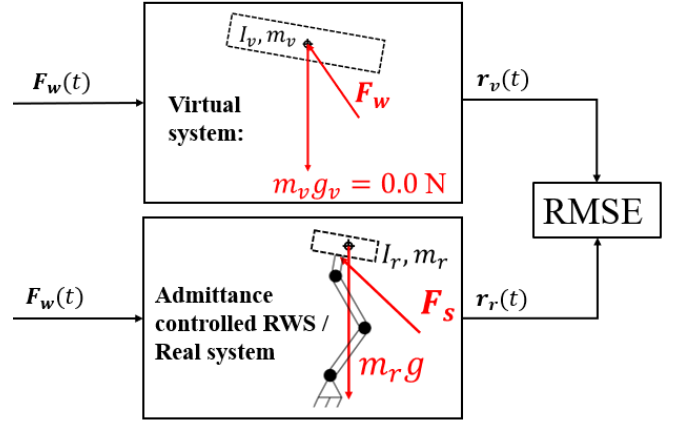


Fig. 8. Block diagram for the second experiment on the HIL setup to verify the simulation abilities of the admittance control loop on the HIL setup. The inputs for the experiment are the user-defined wind loads $F_w(t)$ and the virtual inertia parameters $m_v = 116.75$ kg, $I_v = 38.51$ kgm² and $g_v = 0.0$ m/s². The outputs are the trajectories of the object's CoM in the virtual situation $r_v(t)$ and in the real situation with the RWS $r_r(t)$. The RMSE between $r_v(t)$ and $r_r(t)$ are the final outputs of the experiment.

the three experiments on the HIL setup are now explained. The following section will show the results of these experiments.

III. RESULTS

The results for the experiments conducted on the computer simulation model and the HIL setup will now be shown. Appendix C contains the exact experimental conditions for all experiments.

A. Computer simulation results

1) *Experiment 1:* The first experiment conducted on the computer simulation model is the verification of whether the admittance control loop can simulate desired dynamics and wind loads. Fig. 9 shows the results for this experiment. The found RMSE are:

- RMSE in x is 0.424 N
- RMSE in y is 0.806 N
- RMSE around z is 0.507 Nm

2) *Experiment 2:* The second experiment is the search for the range of possible T_{RWS} . Fig. 10 shows the results. The sample times that result in stable simulations are:

- $T_{RWS} < 0.02$ s

3) *Experiment 3:* The third experiment is the search for the range of possible virtual inertia's (m_v , I_v) while there are no wind loads simulated. The RWS sample time used in these experiments is $T_{RWS} = 0.005$ s. Fig. 11 shows the results graphically, while table I shows them numerically.

4) *Experiment 4:* The fourth experiment researches the dependency between T_{RWS} and the range of possible virtual inertias. Fig. 12 shows the results. Note that this figure only shows the results for a real inertia of $m_r = 14.50$ kg and $I_r = 0.54$ kgm².

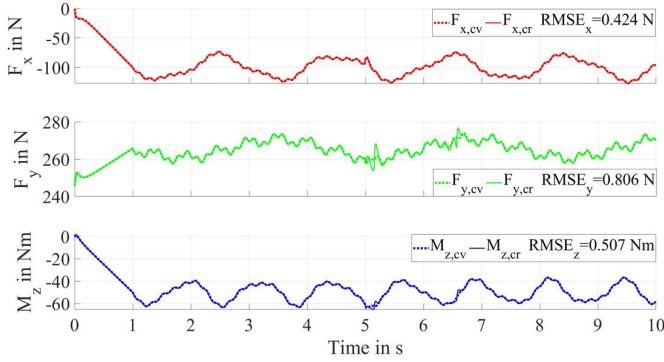


Fig. 9. The results for the first experiment on the computer simulation model. The ObCon forces in the virtual environment F_{ev} and the admittance controlled environment F_{cr} are compared to each other by taking the RMSE of the signals over time. A block diagram of the experiment can be seen in Fig. 6.

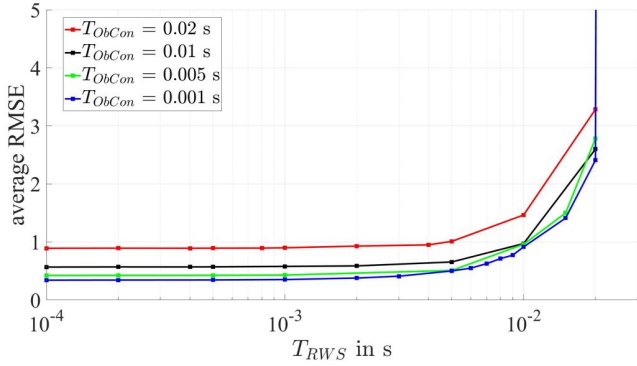


Fig. 10. The results for the second experiment on the computer simulation model. The average RMSE between the ObCon forces in the virtual environment F_{ev} and the admittance controlled environment F_{cr} are plotted against different sample times of the RWS T_{RWS} . This analysis is executed for four different sample times of the ObCon T_{ObCon} .

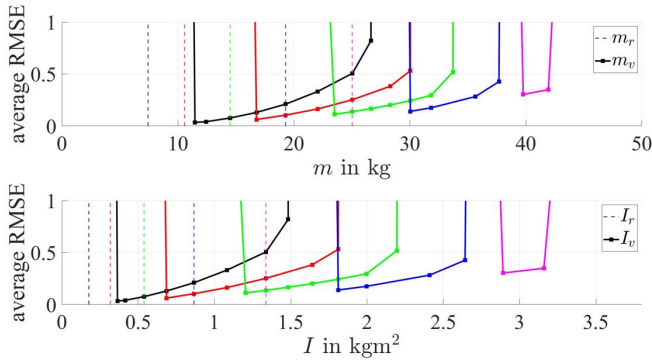


Fig. 11. The results for the third experiment on the computer simulation model. The average RMSE between the ObCon forces in the virtual environment F_{ev} and the admittance controlled environment F_{cr} are plotted against different amounts of virtual inertia (m_v , I_v). This analysis is executed for five different amounts of real object inertia (m_r , I_r), which are indicated in the graphs by the dashed lines. In this experiment there are no wind loads simulated and the sample time is $T_{RWS} = 0.005$ s. The numerical values of the results can be found in table I.

5) *Experiment 5*: The fifth and last experiment on the computer simulation model shows the influence of wind loads on experiment 3. Fig. 13 shows the results graphically, while

TABLE I
NUMERICAL RESULTS FOR THE THIRD EXPERIMENT ON THE COMPUTER SIMULATION MODEL FROM FIG. 11.

Trial	m_r [kg]	I_r [kgm ²]	m_v range [kg]	I_v range [kgm ²]
black	7.42	0.18	11.47 - 26.65	0.36 - 0.82
red	10.57	0.32	16.78 - 30.05	0.69 - 1.81
green	14.50	0.54	23.52 - 33.73	1.20 - 2.20
blue	19.30	0.87	30.05 - 37.69	1.81 - 2.64
magenta	25.05	1.34	39.78 - 41.95	2.89 - 3.16

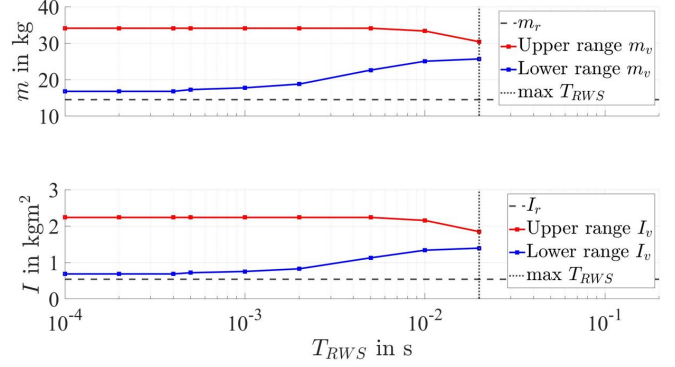


Fig. 12. The results for the fourth experiment on the computer simulation model. The range of possible virtual inertias m_v and I_v are plotted against the sample times for the RWS T_{RWS} . The shown results are obtained in simulations with a real inertia of $m_r = 14.50$ kg and $I_r = 0.54$ kg².

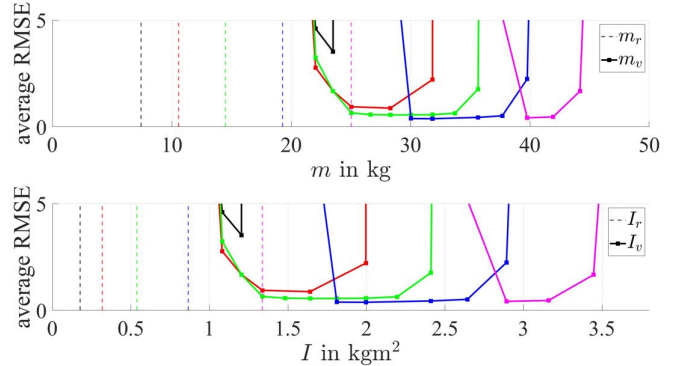


Fig. 13. The results for the fifth experiment on the computer simulation model. The average RMSE between the ObCon forces in the virtual environment F_{ev} and the admittance controlled environment F_{cr} are plotted against different amounts of virtual inertia (m_v , I_v). This analysis is executed for five different amounts of real object inertia (m_r , I_r), which are indicated in the graphs by the dashed lines. In this experiment there are wind loads simulated. Furthermore, the RWS sample time is $T_{RWS} = 0.005$ s. The numerical values of the results can be found in table II.

TABLE II
NUMERICAL RESULTS FOR THE FIFTH EXPERIMENT ON THE COMPUTER SIMULATION MODEL FROM FIG. 13.

Trial	m_r [kg]	I_r [kgm ²]	m_v range [kg]	I_v range [kgm ²]
black	7.42	0.18	22.05 - 23.52	1.08 - 1.20
red	10.57	0.32	22.05 - 31.85	1.08 - 2.00
green	14.50	0.54	22.05 - 35.67	1.08 - 2.41
blue	19.30	0.87	30.05 - 39.78	1.81 - 2.89
magenta	25.05	1.34	39.78 - 44.20	2.89 - 3.45

table II shows them numerically.

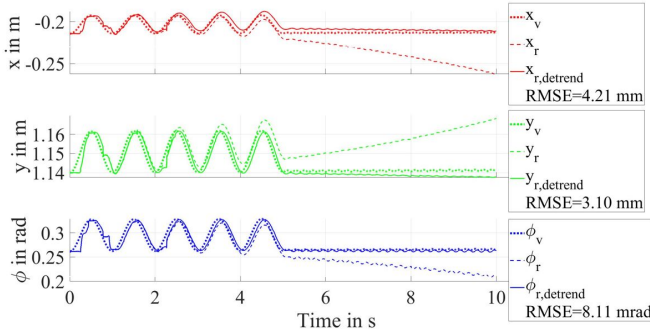


Fig. 14. The results for the second experiment on the HIL setup. The virtual trajectory $\mathbf{r}_v(t)$ and real trajectory $\mathbf{r}_r(t)$ caused by sinusoidal wind loads on a 0-g environment are plotted. Also, the detrended real signal $\mathbf{r}_{r,detrend}(t)$ is plotted. This signal is detrended with the standard drift measured when no wind loads are applied. The sample frequency $\frac{1}{T_{RWS}}$ for this experiment was 2333 Hz. The RMSE in x , in y and in φ are the final metrics for this experiment.

B. Hardware-in-the-loop (HIL) results

1) *Experiment 1*: The first experiment on the HIL setup is the 0-g simulation of a large object in 3 DoF. The results for this experiment are not numerical but shown in the form of a video: CONFIDENTIAL.

2) *Experiment 2*: The second experiment on the HIL setup is the same 0-g simulation but now with sinusoidal wind loads applied and no manipulation by hand. Fig. 14 shows the results of this experiment. The sampling frequency $\frac{1}{T_{RWS}}$ of this experiment was 2333 Hz. It is found that the results of the real trajectory \mathbf{r}_r contain drift. Therefore, these signals are detrended with the standard drift. This standard drift is captured from simulations without wind-loads. The RMSE between the detrended real signal and the virtual signal is taken as a metric. The RMSE are:

- RMSE in x is 4.21 mm
- RMSE in y is 3.10 mm
- RMSE in φ is 8.11 mrad

3) *Experiment 3*: The third and last experiment on the HIL setup analyzes the range of possible sample times of the admittance control loop. Fig. 15 shows the results. This figure shows normalized RMSE. The normalized RMSE is calculated by dividing all RMSE of the experiment with the minimum RMSE of the experiment,

$$\text{Normalized RMSE} = \frac{\text{RMSE}}{\min(\text{RMSE})} \quad (7)$$

The RMSE is normalized in order to be able to compare it to the sample times analysis results from the computer simulation study.

All results from the computer simulation model and the HIL setup have now been shown. The following section discusses these results.

IV. DISCUSSION

Fig. 9 shows the results for the first experiment on the computer simulation model. In these results, it can be seen that an admittance-controlled robot arm can simulate the desired

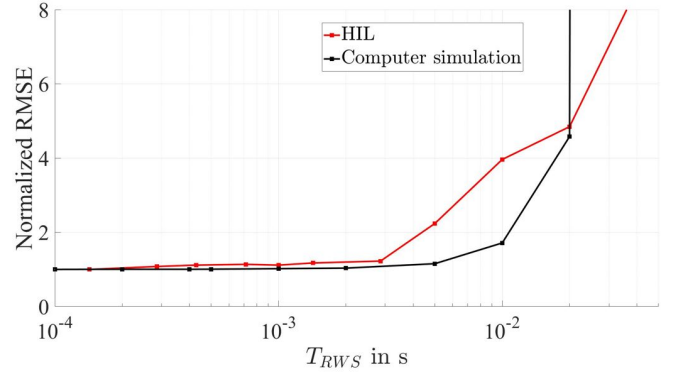


Fig. 15. The results for the third and last experiment on the HIL setup. The sample time of the admittance control loop T_{RWS} is plotted against the normalized error. This error is the RMSE between the virtual object trajectory $\mathbf{r}_v(t)$ and the real object trajectory $\mathbf{r}_r(t)$. The results from the computer simulation model (Fig. 10) are also plotted. The normalized RMSE for both the HIL setup and the computer simulation is found by dividing all RMSE by the minimal RMSE.

inertia of an object while also simulating wind loads on that object. This can be seen because the RMSE between \mathbf{F}_{cv} and \mathbf{F}_{cr} are small with respect to the total forces. The ObCon thus experiences little difference between the virtual and the real situation, which indicates that the dynamics of the virtual and the real situation are equivalent.

The HIL results shown in Fig. 14 confirm the computer simulation results. Again the virtual \mathbf{r}_v and the real \mathbf{r}_r object trajectories are close to each other. However, at the HIL results, a relatively large drift can be seen. In the video results from HIL experiment 1, this drift is visualized by the object's movement before the manipulation by hand. Small inaccuracies in the F/T sensor signal are the cause of this drift. Also, small deviations between the actual real object inertia parameters and the values used for these parameters can influence the drift. The drift could be reduced. For example, by better calibrating the F/T sensor. Also, solving a parameter identification problem can help find the exact real object inertia parameters, thus reducing the drift. However, it is also seen that the HIL simulation is sensitive to drift because it simulates a 0-g environment. Relatively small forces will still cause motions due to the absence of gravity and friction. It is thought that a simulation with gravity is less sensitive to drift. However, future experiments with an ObCon should verify this. Moreover, it is recommended to implement damping into the virtual system by adding air resistance to the virtual EoM.

Fig. 9 and Fig. 14 show that an admittance-controlled industrial robot arm can be used to simulate wind loads on an object while also simulating a desired and higher amount of inertia of that object. This method does have some limitations, for example, in terms of the required sample time of the admittance control loop.

Fig. 10 shows the results for the sample time analysis on the computer simulation model. These results show that the sample time of the ObCon (T_{ObCon}) does not affect the range of possible sample times for the RWS (T_{RWS}). However, it can be seen that at $T_{ObCon} = 0.02$ s the average RMSE are larger. This decline in performance can be explained due to the

performance deterioration of the ObCon itself. I can also be seen that the maximum RWS sample time is $T_{RWS} = 0.02$ s. At larger sample times, the RMSE quickly increases, and the desired wind dynamics simulation are no longer stable. The RMSE are constant below 0.001 s and then start increasing exponentially. Delay between the F_{cv} and F_{cr} signals are the cause of this increase.

The HIL results from Fig. 15 partially confirm the computer simulation results. In the HIL study, it is also seen that at sample times higher than 0.02 s, the simulation starts to vibrate, and the simulation error becomes too high. A difference between the computer simulation results and the HIL result is that the simulation error increases significantly at 0.003 s for the HIL setup and at 0.01 s for the computer simulation.

To summarize, for simulating virtual inertia and wind loads, it is best to use a robot that can change its pose in less than 0.003 s. In other words, the bandwidth of the robot's motion controller and the admittance control loop should be 333 Hz or higher. For frequencies of 333 Hz to 50 Hz, the robot should still simulate the dynamics, but the simulation error will be higher—mainly due to the delay between the virtual and real signals. At frequencies below 50 Hz, the robot will not be able to simulate the dynamics anymore, and the control loop becomes unstable. It is important to note that the control method of the RWS can work with control rates up to 1000 Hz, indicating that the experiments in the range of less than 1000 Hz are valid.

There are also limitations in terms of possible virtual inertia. Fig. 11 and table I show the results for the virtual inertia analysis without wind loads on the computer simulation model. The depicted measurement points are all real/virtual inertia combinations resulting in successful wind dynamics simulations. The first thing that could be seen is that the minimum values of the virtual inertia ranges are higher than the real inertias. For example for real inertia $m_r = 7.42$ kg, $I_r = 0.18$ kgm² the minimum of the possible range of virtual inertia is $m_v = 11.47$ kg, $I_v = 0.36$ kgm². The virtual inertia can never be the same or lower than the real inertia because then the inertia matrix M_{Δ} in the desired dynamics calculations becomes singular or negative. When the virtual inertia is larger than the real inertia, the matrix should not become singular and have positive entries. However, experiment 4 (Fig. 12) shows that the sample time T_{RWS} still makes the desired dynamics calculations unstable when the virtual and real inertias are too close to each other. The lower T_{RWS} , the closer the minimum virtual inertia can be to the real inertia.

There are also upper ranges to the possible virtual inertia simulations. These are caused by the fact that the joint torque limits are reached. The joint torque limits are reached in two different situations. Firstly, the absolute virtual inertia can be too big to simulate with the robot. For example, when too large downward forces must be exerted to simulate a gravitational pull. Alternatively, the joint torque limits can be reached when the difference between the real inertia and the virtual inertia is too big. Furthermore, It can be seen that the larger the difference between the real and virtual inertia, the larger the

RMSE between the ObCon forces are.

Fig. 12 shows that the upper ranges of possible virtual inertia are not as much affected by the sample time T_{RWS} , in comparison to the lower ranges that are affected by T_{RWS} . When a stronger robot is used, the upper ranges are not limited anymore by the joint torque limits. In this case, likely, the upper ranges are also affected by the sample time. This can be analyzed in future research with a stronger robot as RWS.

In Fig. 13 and table II the same virtual inertia analysis results are obtained but now with wind loads. It can be seen that there is now an absolute lower range on the virtual inertia's. Too large forces are needed to simulate wind loads on lightweight objects, which explains the change in the lower range of possible virtual inertias. Further, the possible virtual inertia ranges are approximately the same as in the experiments without wind loads. The wind loads also influence the magnitude of the RMSE, mainly caused by the higher frequencies in the wind loads. These frequencies are too fast to be followed by the robot and therefore increase the RMSE. Because it can be seen in these experiments that the wind loads indeed influence the range of simulation possibilities, it would be interesting to analyze this in future research. The dependencies between magnitude and frequency of the wind loads against virtual inertia can, for example, be plotted.

Unfortunately, the virtual inertia analysis from the computer simulation results can not be verified by results on the HIL setup. There was no ObCon available, and therefore the system could only be tested in a 0-g virtual environment. In zero gravity, much larger virtual inertia's can be simulated by the RWS because it does not have to exert high downward forces to simulate the gravitational pull. It is recommended for future research where an ObCon is available to verify the virtual inertia results from the computer simulation study. This verification can be beneficial for choosing what robot to use as RWS.

Lastly, a discussion can be made about the use of admittance control. This control method is used to simulate satellite dynamics, which is the inspiration for the proposed solution in this research. In space engineering, they mostly use large robotic arms such as the KUKA KR120. These robots do not have torque sensors within the joints. The RWS has torque sensors in the joints and can therefore be commanded joint torques in closed-loop. This gives the ability to use another interaction control method, namely impedance control. This method directly commands forces to the motors based on a user-defined impedance law. A well-defined impedance control law could, in theory, also simulate the desired wind dynamics. [17] describes the principles and strengths/weaknesses of impedance control for robots such as the RWS. An advantage of impedance control for this application is that it is safer in interaction with the environment. This is because joint torques are directly commanded and can therefore be regulated. Another advantage is the lower sample times that can be achieved when directly commanding joint torques with respect to commanding end-effector positions. However, the advantages of admittance control for this application are that it is more intuitive to implement, and it can be used on all different kinds of robot arms. A stronger robot such as the

KUKA KR120 might be required to simulate larger virtual inertia and higher wind loads. No changes in the admittance control loop are needed to switch to this stronger robot.

V. CONCLUSION

- An admittance-controlled industrial robot arm can be used to simulate wind loads on an object while also simulating a desired and higher amount of inertia of that object.
- The bandwidth of the industrial robot's motion controller influences these simulations:
 - The best simulation results are found at frequencies higher than 333 Hz, which means that the robot should be able to change its end-effector position within 0.003 s.
 - At frequencies between 333 Hz and 50 Hz, the simulation is stable, but the simulation error increases.
 - Sampling frequencies lower than 50 Hz result in unstable simulations.
- The range of possible virtual inertia is dependent on multiple aspects:
 - It is dependent on the maximum forces that the robot can apply. The stronger the robot, the higher the virtual inertia can be and the larger the difference between the real and virtual inertia can be.
 - It is dependent on the inertia of the real object. The virtual inertia must always be larger than the real inertia. Therefore, the smaller the real inertia, the smaller the virtual inertia can be.
 - It is dependent on the sampling frequency. The higher the sampling frequency, the closer the virtual inertia can be to the real inertia.
- The sample time analysis is confirmed in a computer simulation study and a HIL study. The virtual inertia analysis is only confirmed in a computer simulation study. For future research, it is recommended to execute the virtual inertia analysis in a HIL study.
- Simulating wind loads is possible with the admittance control loop. However, these wind loads increase the simulation error and affect the range of possible virtual inertias. For future research, it is recommended to analyse this wind load influence in more detail.

REFERENCES

- [1] I. Bayati, A. Facchinetti, A. Fontanella, H. Giberti, and M. Belloli, "A wind tunnel/HIL setup for integrated tests of floating offshore wind turbines," vol. 1037, p. 052025, publisher: IOP Publishing. [Online]. Available: <https://doi.org/10.1088/1742-6596/1037/5/052025>
- [2] S. Chakrabarti, "Chapter 13 – physical modelling of offshore structures."
- [3] F. Aghili and M. Namvar, "Scaling inertia properties of a manipulator payload for 0-g emulation of spacecraft," vol. 28, no. 7, pp. 883–894, publisher: SAGE Publications Ltd STM. [Online]. Available: <https://doi.org/10.1177/0278364908099464>
- [4] T. Boge, T. Wimmer, O. Ma, and T. Tzschichholz, *EPOS – Using Robotics for RvD Simulation of On-Orbit Servicing Missions*, journal Abbreviation: AIAA Modeling and Simulation Technologies Conference 2010 Publication Title: AIAA Modeling and Simulation Technologies Conference 2010.
- [5] J. Artigas, M. De Stefano, W. Rackl, R. Lampariello, B. Brunner, W. Bertleff, R. Burger, O. Porges, A. Giordano, C. Borst, and A. Albu-Schaeffer, "The OOS-SIM: An on-ground simulation facility for on-orbit servicing robotic operations," in *2015 IEEE International Conference on Robotics and Automation (ICRA)*, pp. 2854–2860, ISSN: 1050-4729.
- [6] M. De Stefano, H. Mishra, A. M. Giordano, R. Lampariello, and C. Ott, "A relative dynamics formulation for hardware- in-the-loop simulation of on-orbit robotic missions," vol. 6, no. 2, pp. 3569–3576, conference Name: IEEE Robotics and Automation Letters.
- [7] V. Scheinman, J. M. McCarthy, and J.-B. Song, "Mechanism and actuation," in *Springer Handbook of Robotics*, ser. Springer Handbooks. Springer International Publishing, pp. 68–87. [Online]. Available: https://doi.org/10.1007/978-3-319-32552-1_2
- [8] J. J. Craig, *Introduction to robotics: mechanics and control*, 3/E. Pearson Education India.
- [9] H. Vallery and A. Schwab, *Advanced Dynamics*, 2nd ed. Delft University of Technology.
- [10] W. K. Chung, L.-C. Fu, and T. Kröger, "Motion control," in *Springer Handbook of Robotics*, ser. Springer Handbooks. Springer International Publishing, pp. 164–191. [Online]. Available: https://doi.org/10.1007/978-3-319-32552-1_2
- [11] Y. Nakamura and H. Hanafusa, "Inverse kinematic solutions with singularity robustness for robot manipulator control," vol. 108, no. 3, pp. 163–171. [Online]. Available: <https://doi.org/10.1115/1.3143764>
- [12] T. Yoshikawa, "Manipulability of robotic mechanisms," vol. 4, no. 2, pp. 3–9, publisher: SAGE Publications Ltd STM. [Online]. Available: <https://doi.org/10.1177/027836498500400201>
- [13] N. Hogan, "Impedance control: An approach to manipulation: Part i—theory."
- [14] —, "Impedance control: An approach to manipulation: Part II—implementation."
- [15] —, "Impedance control: An approach to manipulation: Part III—applications."
- [16] K. M. Lynch and F. C. Park, *Modern robotics: mechanics, planning, and control*. Cambridge University Press, OCLC: ocn983881868.
- [17] A. Albu-Schaeffer and G. Hirzinger, "Cartesian impedance control techniques for torque controlled light-weight robots," in *Proceedings 2002 IEEE International Conference on Robotics and Automation (Cat. No.02CH37292)*, vol. 1. IEEE, pp. 657–663. [Online]. Available: <http://ieeexplore.ieee.org/document/1013433/>

Appendix A

Planar computer simulation model

Appendix is confidential. The full version can be requested at: info@deltaxlab.com

Appendix B

Admittance control in 6 Degrees of Freedom (DoF)

Appendix is confidential. The full version can be requested at: info@deltaxlab.com

Appendix C

Experimental conditions

Appendix is confidential. The full version can be requested at: info@deltaxlab.com

References

- [1] I. Bayati, A. Facchinetti, A. Fontanella, H. Giberti, and M. Belloli, “A wind tunnel/HIL setup for integrated tests of floating offshore wind turbines,” vol. 1037, p. 052025, publisher: IOP Publishing. [Online]. Available: <https://doi.org/10.1088/1742-6596/1037/5/052025>
- [2] S. Chakrabarti, “Chapter 13 – physical modelling of offshore structures.”
- [3] F. Aghili and M. Namvar, “Scaling inertia properties of a manipulator payload for 0-g emulation of spacecraft,” vol. 28, no. 7, pp. 883–894, publisher: SAGE Publications Ltd STM. [Online]. Available: <https://doi.org/10.1177/0278364908099464>
- [4] T. Boge, T. Wimmer, O. Ma, and T. Tzschichholz, *EPOS – Using Robotics for RvD Simulation of On-Orbit Servicing Missions*, journal Abbreviation: AIAA Modeling and Simulation Technologies Conference 2010 Publication Title: AIAA Modeling and Simulation Technologies Conference 2010.
- [5] J. Artigas, M. De Stefano, W. Rackl, R. Lampariello, B. Brunner, W. Bertleff, R. Burger, O. Porges, A. Giordano, C. Borst, and A. Albu-Schaeffer, “The OOS-SIM: An on-ground simulation facility for on-orbit servicing robotic operations,” in *2015 IEEE International Conference on Robotics and Automation (ICRA)*, pp. 2854–2860, ISSN: 1050-4729.
- [6] M. De Stefano, H. Mishra, A. M. Giordano, R. Lampariello, and C. Ott, “A relative dynamics formulation for hardware- in-the-loop simulation of on-orbit robotic missions,” vol. 6, no. 2, pp. 3569–3576, conference Name: IEEE Robotics and Automation Letters.
- [7] V. Scheinman, J. M. McCarthy, and J.-B. Song, “Mechanism and actuation,” in *Springer Handbook of Robotics*, ser. Springer Handbooks. Springer International Publishing, pp. 68–87. [Online]. Available: https://doi.org/10.1007/978-3-319-32552-1_2
- [8] J. J. Craig, *Introduction to robotics: mechanics and control, 3/E*. Pearson Education India.
- [9] H. Vallery and A. Schwab, *Advanced Dynamics*, 2nd ed. Delft University of Technology.
- [10] W. K. Chung, L.-C. Fu, and T. Kröger, “Motion control,” in *Springer Handbook of Robotics*, ser. Springer Handbooks. Springer International Publishing, pp. 164–191. [Online]. Available: https://doi.org/10.1007/978-3-319-32552-1_2

-
- [11] Y. Nakamura and H. Hanafusa, “Inverse kinematic solutions with singularity robustness for robot manipulator control,” vol. 108, no. 3, pp. 163–171. [Online]. Available: <https://doi.org/10.1115/1.3143764>
- [12] T. Yoshikawa, “Manipulability of robotic mechanisms,” vol. 4, no. 2, pp. 3–9, publisher: SAGE Publications Ltd STM. [Online]. Available: <https://doi.org/10.1177/027836498500400201>
- [13] N. Hogan, “Impedance control: An approach to manipulation: Part i—theory.”
- [14] —, “Impedance control: An approach to manipulation: Part II—implementation.”
- [15] —, “Impedance control: An approach to manipulation: Part III—applications.”
- [16] K. M. Lynch and F. C. Park, *Modern robotics: mechanics, planning, and control*. Cambridge University Press, OCLC: ocn983881868.
- [17] A. Albu-Schaffer and G. Hirzinger, “Cartesian impedance control techniques for torque controlled light-weight robots,” in *Proceedings 2002 IEEE International Conference on Robotics and Automation (Cat. No.02CH37292)*, vol. 1. IEEE, pp. 657–663. [Online]. Available: <http://ieeexplore.ieee.org/document/1013433/>

Glossary

List of Acronyms

BMD	BioMechanical Design
BR	BioRobotics
CoM	Centre of Mass
DC	Direct Current
DoF	Degree(s) of Freedom
emf	electromotive force(s)
EoM	Equations of Motion
FBD	Free Body Diagram(s)
FK	Forward Kinematics
F/T	Force/Torque
HIL	Hardware-In-the-Loop
ME	Mechanical Engineering
ObCon	Object Controller
OOS	On-Orbit Servicing
RMSE	Root Mean Squared Error(s)
RWS	Robotic Wind Simulator
TU Delft	Delft University of Technology
UDP	User Datagram Protocol
X-Laboratory	Delta Labs B.V.
3mE	Mechanical, Maritime and Materials Engineering

List of Symbols

$\tau(\mathbf{V}_a, \dot{\mathbf{q}})$	Motor torques after gearing as a function of armature voltages and joint velocities
$\ddot{\varphi}_\bullet$	Angular acceleration of object with subscript \bullet
$\dot{\theta}$	Motor velocity after gearing
$\dot{\theta}_m$	Motor velocity
τ	Motor torque after gearing
τ_m	Motor torque
$\theta_1 \dots \theta_3$	Joint angles
φ	Rotation around z-axis in 3 DoF
φ_r	Real object's CoM orientation around the z-axis
$\ddot{\mathbf{q}}$	Joint accelerations
$\ddot{\mathbf{r}}_{d\{w\}}$	Desired Cartesian accelerations described in the world frame
$\dot{\mathbf{q}}$	Joint velocities
$\dot{\mathbf{r}}_{d\{w\}}$	Desired Cartesian velocities described in the world frame
$\mathbf{C}(\mathbf{q}, \dot{\mathbf{q}})$	Coriolis and centrifugal forces as a function of joint angles
$\mathbf{F}_w(t)$	Wind load input over time
\mathbf{F}_{cr}	ObCon forces in the real environment
\mathbf{F}_{cv}	ObCon forces in the virtual environment
$\mathbf{F}_{r\{r\}}$	Measured forces and torque of the object's CoM described in the sensor frame
$\mathbf{F}_{r\{w\}}$	Measured forces and torque of the object's CoM described in the world frame
$\mathbf{F}_{s\{s\}}$	F/T sensor forces and torque described in the sensor frame
$\mathbf{F}_{w\{w\}}$	Wind forces and torque described in the world frame
$\mathbf{FK}(\mathbf{q})$	Forward kinematics as a function of joint angles
$\mathbf{G}(\mathbf{q})$	Gravitational forces as function of joint angles
\mathbf{G}_Δ	Virtual gravitational vector minus the real gravitational vector
$\mathbf{J}(\mathbf{q})$	Jacobian as a function of joint angles
$\mathbf{J}^{-1}(\mathbf{q})$	Inverse Jacobian as a function of joint angles
$\mathbf{M}(\mathbf{q})$	Inertia matrix as a function of joint angles
\mathbf{M}_Δ	Virtual inertia matrix minus the real inertia matrix
$\mathbf{p}_o(t)$	Reference trajectory for the ObCon
\mathbf{q}	Joint angles
$\mathbf{r}_r(t)$	Real object's CoM trajectory
$\mathbf{r}_v(t)$	Virtual object's CoM trajectory
$\mathbf{r}_{d\{w\}}$	Desired Cartesian pose described in the world frame
$\mathbf{r}_{r,\text{detrend}}(t)$	$[x_{r,\text{detrend}}, y_{r,\text{detrend}}, \varphi_{r,\text{detrend}}]^T$ is the detrended real object's CoM trajectory.
\mathbf{R}	Rotation matrix of $\mathbf{F}_{r\{r\}}$ to $\mathbf{F}_{r\{w\}}$
\mathbf{T}	Transformation matrix of $\mathbf{F}_{s\{s\}}$ to $\mathbf{F}_{r\{r\}}$
\ddot{x}_\bullet	Acceleration in x-direction of object with subscript \bullet

\ddot{y}_{\bullet}	Acceleration in y-direction of object with subscript \bullet
$\{\bullet\}$	Frame notation
$\{r\}$	Object frame
$\{s\}$	F/T sensor frame
$\{w\}$	World frame
$A_1 \dots A_7$	Axes of the RWS
$A'_1 \dots A'_3$	Axes of the three-link manipulator computer simulation model
b_l	Friction in manipulator link
b_m	Friction in DC motor
d_x	Object's CoM distance in x described in the sensor frame
d_y	Object's CoM distance in y described in the sensor frame
$F_{x,\bullet}$	Force in x of the force with subscript \bullet
$F_{y,\bullet}$	Force in y of the force with subscript \bullet
g	Real gravitational acceleration
g_v	Virtual gravitational acceleration
I_l	Moment of inertia manipulator link
I_m	Moment of inertia DC motor
I_r	Real object mass moment of inertia
I_v	Virtual object mass moment of inertia
$l_1 \dots l_3$	Link lengths of the three-link manipulator computer simulation model
$l_a \dots l_g$	Link lengths of the RWS
m_r	Real object mass
m_v	Virtual object mass
$M_{z,\bullet}$	Moment around z of the moment with subscript \bullet
r	Gearing ratio
T_{dyn}	Sample time of the forward dynamics calculations
T_{joint}	Sample time of the joint torque controllers
T_{ObCon}	Sample time of the ObCon
T_{RWS}	Sample time of the admittance control loop and the Cartesian motion controller of the RWS
x	X-coordinate of a frame
y	Y-coordinate of a frame
z	Z-coordinate of a frame
\int	Integrator
[Hz]	Hertz
[kg]	Kilogram(s)
[m]	Meter(s)
[mm]	Millimeter(s)
[mrad]	Milliradian(s)
[N]	Newton(s)
[rad]	Radian(s)
[s]	Second(s)

